COMMUN. MATH. SCI.
Vol. 18, No. 8, pp. 2149–2168

OPERATOR SPLITTING BASED CENTRAL-UPWIND SCHEMES FOR SHALLOW WATER EQUATIONS WITH MOVING BOTTOM TOPOGRAPHY*

ALINA CHERTOCK†, ALEXANDER KURGANOV‡, AND TONG WU§

Abstract. In this paper, we develop a robust and efficient numerical method for shallow water equations with moving bottom topography. The model consists of the Saint-Venant system governing the water flow coupled with the Exner equation for the sediment transport. One of the main difficulties in designing good numerical methods for such models is related to the fact that the speed of water surface gravity waves is typically much faster than the speed at which the changes in the bottom topography occur. This imposes a severe stability restriction on the size of time steps, which, in turn, leads to excessive numerical diffusion that affects the computed bottom structure. In order to overcome this difficulty, we develop an operator splitting approach for the underlying coupled system, which allows one to treat slow and fast waves in a different manner and using different time steps. Our method is based on the application of a finite-volume central-upwind scheme introduced in [A. Kurganov and G. Petrova, Commun. Math. Sci., 5:133–160, 2007], and incorporates a staggered grid strategy needed for a proper approximation of the bottom topography function. A number of one- and two-dimensional numerical examples are presented to demonstrate the performance of the proposed method.

Keywords. Saint Venant system of shallow water equations; moving bottom topography; Exner equation; operator splitting method, semi-discrete central-upwind schemes.

AMS subject classifications. 65M08, 76M12; 86-08; 86A05; 35L65.

1. Introduction

Shallow water models are widely used as a mathematical framework to study water flows in rivers and coastal areas as well as to investigate a variety of phenomena in atmospheric sciences and oceanography. One of the classical shallow water models is the Saint-Venant (SV) system [11], which in the two-dimensional (2-D) case can be written in the following form:

$$\begin{cases} h_t+(hu)_x+(hv)_y=0,\\ (hu)_t+\left(hu^2+\dfrac{g}{2}h^2\right)_x+(huv)_y=-ghB_x,\\ (hv)_t+(huv)_x+\left(hv^2+\dfrac{g}{2}h^2\right)_y=-ghB_y. \end{cases} \tag{1.1}$$

Here, $h(x,y,t)$ is the fluid depth above the bottom, $u(x,y,t)$ and $v(x,y,t)$ are the x- and y-velocities, g is the constant gravitational acceleration, and $B(x,y)$ is the bottom topography function. More realistic shallow water models may also include, among other things, Coriolis and wind forces, friction terms, horizontal and vertical density variations, viscous, dispersive and turbulent effects.

In this paper, we consider the case, which appears in many practical situations, when the bottom topography $B=B(x,y,t)$ is time-dependent due to erosion, sediment

*Received: September 22, 2019; Accepted (in revised form): June 07, 2020. Communicated by Shi Jin.

†Department of Mathematics, North Carolina State University, Raleigh, NC, 27695, USA (chertock@math.ncsu.edu).

‡Department of Mathematics and SUSTech International Center for Mathematics, Southern University of Science and Technology, Shenzhen, 518055, China (alexander@sustech.edu.cn).

§Department of Mathematics, The University of Texas at San Antonio, San Antonio, TX 78249, USA (tong.wu@utsa.edu).

transport, dam breaks, floods and submarine landslides; see, e.g., [20, 21, 40, 44, 45, 50, 51, 57, 58]. The simplest way to model the bed load sediment transport was proposed in [14, 20]. According to this approach the bottom topography function satisfies the following equation:

$$B_t + A\left[u(u^2+v^2)^{(m-1)/2}\right]_x + A\left[v(u^2+v^2)^{(m-1)/2}\right]_y = 0, \tag{1.2}$$

where A is a constant, which accounts for the porosity of the sediment layer and effects of sediment grain size and kinematic viscosity, and $m \in [1,4]$ is a constant. The values of A and m are often obtained from experimental data. If A is zero, there is no sediment transport, and the system (1.1), (1.2) reduces to the classical SV system (1.1). The interaction between the sediment and the water is weak when A is small and strong when A is large. One thing to note about this model is that there is no threshold necessary to initiate motion and sediment bed load transport will begin with the fluid motion.

The system (1.1), (1.2) is a system of hyperbolic balance laws, which admits non-smooth solutions. Therefore, a numerical method for (1.1), (1.2) should be based on a shock-capturing scheme. In addition, a good numerical method should be capable of accurately capturing both the steady states and their small perturbations (quasi-steady flows). This property ensures that the scheme suppresses the appearance of unphysical waves of magnitude proportional to the grid size, which are normally present when computing quasi-steady states. From a practical point of view, one of its most important steady-state solutions of the system (1.1), (1.2) is a "lake at rest" one:

$$u = v \equiv 0, \quad h + B \equiv \text{Const}, \quad B(x,y,t) = B(x,y,0) \quad \forall t.$$

The methods that exactly preserve such solutions are called well-balanced; see [1,3,27,30, 31, 34, 39, 49, 59] for some well-balanced methods for the SV system (1.1). Even though a rigorous stability analysis of these schemes is usually out of reach, they typically produce highly accurate approximations of quasi-steady solutions.

An additional difficulty in solving the coupled system (1.1), (1.2) numerically is associated with the fact that the speed of water surface gravity waves is typically much faster than the speed at which the changes in the bottom topography occur. This imposes a severe stability restriction on the size of time steps, which, in turn, leads to excessive numerical diffusion that affects the computed bottom structure; see, e.g., [2, 5, 13, 23, 24].

In this paper, we overcome the latter difficulty by developing an operator splitting method (see, e.g., [25, 42, 52, 55]) for the system (1.1), (1.2) and its one-dimensional (1-D) version. To this end, we split the SV system (1.1) from the Exner equation (1.2). The size of splitting time steps will be made inversely proportional to the amplitude of a smaller eigenvalue of the Jacobians of the extended system (1.1), (1.2). We will then follow the approach that was utilized in the framework of the fast explicit operator splitting method [8, 9]: each SV splitting substep will consist of several smaller time evolution steps. This way we will ensure the stability of the SV substeps, while large Exner splitting substeps will prevent excessive numerical dissipation, which may severely affect the resolution of the bottom topography, especially in the case when B is discontinuous.

Each of the splitting substeps will be carried out using a second-order well-balanced central-upwind (CU) scheme. High-resolution Godunov-type semi-discrete CU schemes were originally developed in [32, 33, 35] as a universal method for general multidimensional systems of hyperbolic conservation laws. CU schemes belong to a family of

Riemann-problem-solver-free non-oscillatory central schemes and thus can be applied as a "black-box" solver to the Exner Equation (1.2). The CU schemes have also been extended to systems of balance laws and applied to the SV system (1.1) in a series of works. In this paper, we will implement the well-balanced CU scheme proposed in [34]. Since this scheme uses a continuous piecewise linear (or bilinear) reconstruction of the bottom topography, the Exner equation will be solved on a staggered grid so that the point values of B will be evolved in time at every finite-volume cell interface, while the cell averages of h, hu and hv will be evolved inside each cell.

The paper is organized as follows. The 1-D numerical scheme is presented in §2. First, in §2.1, we describe the operator splitting approach. We then present the semi-discretizations of the hydrodynamic (§2.2) and morphodynamic (§2.3) subsystems. Finally, we summarize the 1-D algorithm in §2.4. The 2-D scheme is presented in §3 in a similar way: we introduce the operator splitting method (§3.1), semi-discretizations of the hydrodynamic (§3.2) and morphodynamic (§3.3) subsystems, and the general algorithm (§3.4). The proposed 1-D and 2-D schemes are tested on six numerical examples in §4. Some concluding remarks can be found in §5.

2. One-dimensional numerical scheme

We begin by considering a 1-D version of the SV system (1.1):

$$\begin{cases} h_t+(hu)_x=0,\\ (hu)_t+\left(hu^2+\dfrac{g}{2}h^2\right)_x=-ghB_x, \end{cases} \tag{2.1}$$

coupled with the 1-D version of the Exner Equation (1.2):

$$B_t+A(u^3)_x=0, \tag{2.2}$$

where we have taken $m=3$ (this value of m will be used throughout the paper). Following [31, 34], we rewrite the SV system (2.1) in terms of the equilibrium variables $w:=h+B$ and $q:=hu$:

$$\begin{cases} w_t+(q+Au^3)_x=0,\\ q_t+\left(\dfrac{q^2}{w-B}+\dfrac{g}{2}(w-B)^2\right)_x=-g(w-B)B_x. \end{cases} \tag{2.3}$$

The eigenvalues of the Jacobian of the system (2.3), (2.2) (or (2.1), (2.2)) are the three roots of the following characteristic polynomial:

$$P(\lambda)=\lambda^3-2u\lambda^2+\left(u^2-3Agu^2-gh\right)\lambda+3Agu^3. \tag{2.4}$$

It can be shown (see, e.g., [47]) that the roots of (2.4) are real, distinct and given by

$$\lambda^{(\ell)}=2\sqrt{-Q}\cos\left(\frac{1}{3}\left[\arccos\left(\frac{R}{\sqrt{-Q^3}}\right)+2\pi\ell\right]\right)+\frac{2}{3}u,\quad \ell=0,1,2, \tag{2.5}$$

provided the polynomial determinant $D=Q^3+R^2<0$, where

$$Q=-\frac{1}{9}\left[u^2+3g(h+3Au^2)\right]\quad\text{and}\quad R=\frac{1}{54}\left[9gu(2h-3Au^2)-2u^3\right]. \tag{2.6}$$

A straightforward computation leads to the following formula for determinant D:

$$D=-\frac{g}{108}\left[4h(u^2-gh)^2+108A^3g^3u^6+9A^2gu^4(12gh+u^2)+12Aghu^2(36gh+5u^2)\right],$$

which clearly indicates that indeed $D<0$ for any $h>0$.

One may show that in (2.5), $\lambda^{(2)}$ is always between $\lambda^{(0)}$ and $\lambda^{(1)}$. As it was mentioned above, the speed of water surface gravity waves is in many cases much faster than the speed at which the bottom topography moves and as a result, $\lambda^{(0)}$ and $\lambda^{(1)}$ are typically of a much larger magnitude than $\lambda^{(2)}$. For instance, in a subcritical case with a relatively small u, $\lambda^{(0)}$ and $\lambda^{(1)}$ are typically close to $u\pm\sqrt{gh}$, while $\lambda^{(2)}$ is very small (in a supercritical case, $\lambda^{(0)}$ and $\lambda^{(1)}$ are quite different from $u\pm\sqrt{gh}$, and $\lambda^{(2)}$ is close to u). As a result, the CFL time step restriction, which is based on $\max\{|\lambda^{(0)}|,|\lambda^{(1)}|\}$, may result in excessive numerical diffusion that would affect the computed (slowly moving) bottom structure. This naturally leads to the idea of applying an operator splitting approach, in which the numerical methods for (2.3) and (2.2) can be based on different local propagation speeds.

2.1. Operator splitting. In this section, we describe the proposed operator splitting method. To this end, we consider the following two subsystems:

$$\begin{cases}\boldsymbol{U}_t+\boldsymbol{F}(\boldsymbol{U},B)_x=\boldsymbol{S}(\boldsymbol{U},B),\\ B_t=0\end{cases}\tag{2.7}$$

with

$$\boldsymbol{U}=\begin{pmatrix}w\\ q\end{pmatrix},\quad \boldsymbol{F}(\boldsymbol{U},B)=\begin{pmatrix}q+Au^3\\ \dfrac{q^2}{w-B}+\dfrac{g}{2}(w-B)^2\end{pmatrix},\quad \boldsymbol{S}(\boldsymbol{U},B)=\begin{pmatrix}0\\ -g(w-B)B_x\end{pmatrix},\tag{2.8}$$

and

$$\begin{cases}\boldsymbol{U}_t=\boldsymbol{0},\\ B_t+A(u^3)_x=0.\end{cases}\tag{2.9}$$

The subsystem (2.7)–(2.8) represents slightly modified shallow water equations with the time-independent bottom topography, and it will be referred to as the *hydrodynamic* subsystem. The subsystem (2.9) represents the Exner equation with the time-independent water depth and velocity, and it will be referred to as the *morphodynamic* subsystem.

Assuming $\boldsymbol{U}(x,t)$ and $B(x,t)$ are available at time t, let $\mathcal{S}_H$ and $\mathcal{S}_M$ denote the solution operators for the subsystems (2.7)–(2.8) and (2.9), respectively. Then, an approximate solution at the next time level $t+\Delta t$ can be obtained by using the following second-order Strang operator splitting method:

$$\begin{pmatrix}\boldsymbol{U}(x,t+\Delta t)\\ B(x,t+\Delta t)\end{pmatrix}\approx\mathcal{S}_H(\Delta t/2)\mathcal{S}_M(\Delta t)\mathcal{S}_H(\Delta t/2)\begin{pmatrix}\boldsymbol{U}(x,t)\\ B(x,t)\end{pmatrix}.\tag{2.10}$$

For a practical implementation, one needs to choose a proper splitting time step Δt and replace the solution operators, $\mathcal{S}_H$ and $\mathcal{S}_M$, in (2.10) with their finite-volume discretizations, which will be described in detail in §2.2 and §2.3.

REMARK 2.1. The proposed operator splitting method can be extended to the third order of accuracy by implementing the algorithm proposed in [25]. We also refer the reader to [38,60] for higher-order operator splitting methods. Notice, however, that it can be shown that splitting methods of orders higher than three will require some negative time increments [53], which may cause numerical instability when time irreversible (dissipative) systems like the ones studied here are solved.

2.2. Semi-discretization of the hydrodynamic subsystem. We denote by $C_j:=[x_{j-\frac12},x_{j+\frac12}]$ the uniform cells of size Δx centered at x_j. The computed solution, realized in terms of the cell averages $\overline{\boldsymbol{U}}_j(t)\approx\frac{1}{\Delta x}\int_{C_j}\boldsymbol{U}(x,t)\,\mathrm{d}x$ and point values $B_{j+\frac12}(t)\approx B(x_{j+\frac12},t)$, is assumed to be known at a given time t (for the sake of brevity, we will omit the time dependence of all of the indexed quantities in the rest of this paper). The cell averages are evolved in time according to the well-balanced semi-discretization from [34] (note that this can be done since B is time-independent in the system (2.7)–(2.8)):

$$\frac{\mathrm{d}}{\mathrm{d}t}\overline{\boldsymbol{U}}_j=-\frac{\boldsymbol{H}_{j+\frac12}-\boldsymbol{H}_{j-\frac12}}{\Delta x}+\overline{\boldsymbol{S}}_j, \tag{2.11}$$

where

$$\boldsymbol{H}_{j+\frac12}=\frac{a^+_{j+\frac12}\boldsymbol{F}\big(\boldsymbol{U}^-_{j+\frac12},B_{j+\frac12}\big)-a^-_{j+\frac12}\boldsymbol{F}\big(\boldsymbol{U}^+_{j+\frac12},B_{j+\frac12}\big)}{a^+_{j+\frac12}-a^-_{j+\frac12}}+\frac{a^+_{j+\frac12}a^-_{j+\frac12}}{a^+_{j+\frac12}-a^-_{j+\frac12}}\Big[\boldsymbol{U}^+_{j+\frac12}-\boldsymbol{U}^-_{j+\frac12}\Big] \tag{2.12}$$

are the central-upwind numerical fluxes and

$$\overline{\boldsymbol{S}}_j=\left(0,-g\frac{h^-_{j+\frac12}+h^+_{j-\frac12}}{2}\cdot\frac{B_{j+\frac12}-B_{j-\frac12}}{\Delta x}\right)^\top$$

are the approximated cell averages of the geometric source term $\boldsymbol{S}$.

In (2.12),

$$\boldsymbol{U}^+_{j+\frac12}=\overline{\boldsymbol{U}}_{j+1}-\frac{\Delta x}{2}(\boldsymbol{U}_x)_{j+1}\quad\text{and}\quad\boldsymbol{U}^-_{j+\frac12}=\overline{\boldsymbol{U}}_j+\frac{\Delta x}{2}(\boldsymbol{U}_x)_j \tag{2.13}$$

are the reconstructed right- and left-sided point values of $\boldsymbol{U}$, which are monotonized using the generalized minmod limiter (see, e.g., [41,46,54,56]):

$$(\boldsymbol{U}_x)_j=\mathrm{minmod}\left(\theta\frac{\overline{\boldsymbol{U}}_j-\overline{\boldsymbol{U}}_{j-1}}{\Delta x},\frac{\overline{\boldsymbol{U}}_{j+1}-\overline{\boldsymbol{U}}_{j-1}}{2\Delta x},\theta\frac{\overline{\boldsymbol{U}}_{j+1}-\overline{\boldsymbol{U}}_j}{\Delta x}\right),\quad\theta\in[1,2], \tag{2.14}$$

where the minmod function is defined by

$$\mathrm{minmod}(z_1,\ldots,z_j):=\begin{cases}\min\limits_j\{z_j\}, & \text{if } z_j>0\ \ \forall j,\\ \max\limits_j\{z_j\}, & \text{if } z_j<0\ \ \forall j,\\ 0, & \text{otherwise.}\end{cases} \tag{2.15}$$

The parameter θ in (2.14) is used to control the amount of the numerical viscosity, with larger θ values resulting in less dissipative, but slightly more oscillatory results.

Finally, the local one-sided speeds of propagation $a^+_{j+\frac12}$ and $a^-_{j+\frac12}$ in (2.12) are obtained from the largest and smallest eigenvalues of the Jacobian of the original unsplit system (2.3), (2.2) and are given by

$$a^+_{j+\frac12}=\max\Big\{\lambda^{(0)+}_{j+\frac12},\lambda^{(1)+}_{j+\frac12},\lambda^{(0)-}_{j+\frac12},\lambda^{(1)-}_{j+\frac12},0\Big\},\quad a^-_{j+\frac12}=\min\Big\{\lambda^{(0)+}_{j+\frac12},\lambda^{(1)+}_{j+\frac12},\lambda^{(0)-}_{j+\frac12},\lambda^{(1)-}_{j+\frac12},0\Big\},$$

where $\lambda^{(0)\pm}_{j+\frac12}$ and $\lambda^{(1)\pm}_{j+\frac12}$ are computed using (2.5), (2.6) with $h=h^\pm_{j+\frac12}=w^\pm_{j+\frac12}-B_{j+\frac12}$ and $u=q^\pm_{j+\frac12}/h^\pm_{j+\frac12}$, respectively.

2.3. Semi-discretization of the morphodynamic subsystem. In this section, we describe the semi-discrete central-upwind scheme for the system (2.9), which is discretized on a staggered grid with $C_{j+\frac{1}{2}}=[x_j,x_{j+1}]$. To this end, we first project the data, $\{\overline{\boldsymbol{U}}_j\}$, obtained at the hydrodynamic splitting step onto the staggered grid as it was done, for example, in [26]:

$$\overline{\boldsymbol{U}}_{j+\frac{1}{2}}=\frac{\overline{\boldsymbol{U}}_j+\overline{\boldsymbol{U}}_{j+1}}{2}-\frac{\Delta x}{8}\Big[(\boldsymbol{U}_x)_{j+1}-(\boldsymbol{U}_x)_j\Big],$$

where the slopes $(\boldsymbol{U}_x)_j$ are computed using (2.14). $B_{j+\frac{1}{2}}$ are then evolved in time according to the following semi-discretization (note that at this splitting stage u is time-independent):

$$\frac{\mathrm{d}}{\mathrm{d}t}B_{j+\frac{1}{2}}=-\frac{H_{j+1}-H_j}{\Delta x},\tag{2.16}$$

where

$$H_j=A\frac{b_j^+\big(u_j^-\big)^3-b_j^-\big(u_j^+\big)^3}{b_j^+-b_j^-}+\frac{b_j^+b_j^-}{b_j^+-b_j^-}\big[B_j^+-B_j^-\big]\tag{2.17}$$

are the central-upwind numerical fluxes.

In (2.17),

$$B_j^+=B_{j+\frac{1}{2}}-\frac{\Delta x}{2}(B_x)_{j+\frac{1}{2}}\quad\text{and}\quad B_j^-=B_{j-\frac{1}{2}}+\frac{\Delta x}{2}(B_x)_{j-\frac{1}{2}}$$

are the reconstructed right- and left-sided point values of B, which, as before, are computed using the generalized minmod limiter:

$$(B_x)_{j+\frac{1}{2}}=\text{minmod}\left(\theta\frac{B_{j+\frac{1}{2}}-B_{j-\frac{1}{2}}}{\Delta x},\frac{B_{j+\frac{3}{2}}-B_{j-\frac{1}{2}}}{2\Delta x},\theta\frac{B_{j+\frac{3}{2}}-B_{j+\frac{1}{2}}}{\Delta x}\right),\quad\theta\in[1,2],$$

where the minmod function is defined by (2.15). The reconstructed point values $w_j^\pm$ and $q_j^\pm$, obtained in a similar manner, are used to calculate $u_j^\pm=q_j^\pm/(w_j^\pm-B_j^\pm)$.

Finally, b_j^+ and b_j^- are local one-sided speeds of propagation, which are obtained using the middle eigenvalue of the Jacobian of the original unsplit system (2.3), (2.2) and are given by

$$b_j^+=\max\Big\{\lambda_j^{(2)+},\lambda_j^{(2)-},0\Big\},\quad b_j^-=\min\Big\{\lambda_j^{(2)+},\lambda_j^{(2)-},0\Big\},$$

where $\lambda_j^{(2)\pm}$ are computed using (2.5), (2.6) with $h=w_j^\pm-B_j^\pm$ and $u=u_j^\pm$, respectively.

REMARK 2.2. The ODE systems (2.11) and (2.16) are numerically solved using the three-stage third-order strong-stability preserving (SSP) Runge-Kutta method (see, e.g., [18,19]).

2.4. Summary of the algorithm. In this section, we summarize one time step of the splitting method assuming that at a certain time level t the computed quantities $\{\overline{w}_j\}$, $\{\overline{q}_j\}$ and $\big\{B_{j+\frac{1}{2}}\big\}$ are available.

Step 1. Compute $w_{j+\frac{1}{2}}^\pm$ and $q_{j+\frac{1}{2}}^\pm$ using (2.13)–(2.15).

Step 2. Compute

$$b_{\max} := \max_j \left\{ \max \left\{ \left| \lambda^{(2)+}_{j+\frac{1}{2}} \right|, \left| \lambda^{(2)-}_{j+\frac{1}{2}} \right| \right\} \right\},$$

where $\lambda^{(2)\pm}_{j+\frac{1}{2}}$ are computed using (2.5), (2.6) with $h = w^{\pm}_{j+\frac{1}{2}} - B_{j+\frac{1}{2}}$ and $u = q^{\pm}_{j+\frac{1}{2}} / (w^{\pm}_{j+\frac{1}{2}} - B_{j+\frac{1}{2}})$, respectively.

Step 3. Choose the splitting time step Δt based on the CFL-type condition for the morphodynamic subsystem:

$$\Delta t = \mathcal{K} \frac{\Delta x}{b_{\max}}, \tag{2.18}$$

where $\mathcal{K}$ is a CFL constant, which according to the stability restriction of central-upwind schemes is supposed to be smaller than $1/2$; see, e.g., [29, 30].

Step 4. Evolve $\left\{ \overline{\boldsymbol{U}}_j \right\}$ by numerically solving the ODE system (2.11) from time level t to $t + \Delta t/2$ with the time step Δt_H being constrained by the following CFL-like condition:

$$\Delta t_H \le \mathcal{K} \frac{\Delta x}{a_{\max}}, \quad a_{\max} := \max_j \left\{ \max \left\{ a^{+}_{j+\frac{1}{2}}, -a^{-}_{j+\frac{1}{2}} \right\} \right\}. \tag{2.19}$$

Denote the obtained solution by $\left\{ \overline{\boldsymbol{U}}^{*}_j \right\}$.

Step 5. Evolve $\left\{ B_{j+\frac{1}{2}} \right\}$ by numerically solving the ODE system (2.16) from time level t to $t + \Delta t$.

Step 6. Evolve $\left\{ \overline{\boldsymbol{U}}^{*}_j \right\}$ by numerically solving the ODE system (2.11) from time level $t + \Delta t/2$ to $t + \Delta t$ with the time step Δt_H being constrained by (2.19).

Step 7. Set $t = t + \Delta t$ and go to Step 1.

3. Two-dimensional numerical scheme

We first take $m = 3$ and rewrite the system (1.1), (1.2) in terms of B and the equilibrium variables w, $q := hu$ and $p := hv$ as follows:

$$\begin{cases} w_t + \left(q + Au(u^2+v^2) \right)_x + \left(p + Av(u^2+v^2) \right)_y = 0, \\ q_t + \left(\dfrac{q^2}{w-B} + \dfrac{g}{2}(w-B)^2 \right)_x + \left(\dfrac{qp}{w-B} \right)_y = -g(w-B)B_x, \\ p_t + \left(\dfrac{qp}{w-B} \right)_x + \left(\dfrac{p^2}{w-B} + \dfrac{g}{2}(w-B)^2 \right)_y = -g(w-B)B_y, \\ B_t + A\left(u(u^2+v^2) \right)_x + A\left(v(u^2+v^2) \right)_y = 0. \end{cases} \tag{3.1}$$

The eigenvalues of the Jacobian of the system (3.1) in the x-direction are u and the three roots of the following characteristic polynomial:

$$P_1(\lambda) = \lambda^3 - 2u\lambda^2 + [u^2 - Ag(3u^2+v^2) - gh]\lambda + Ag(3u^3 + uv^2).$$

The eigenvalues of the Jacobian of the system (3.1) in the y-direction are v and the three roots of the following characteristic polynomial:

$$P_2(\mu) = \mu^3 - 2v\mu^2 + [v^2 - Ag(3v^2+u^2) - gh]\mu + Ag(3v^3 + vu^2).$$

It can be shown that similarly to the 1-D case, the roots of both P_1 and P_2 are real, distinct and given by

$$\lambda^{(\ell)} = 2\sqrt{-Q_\lambda}\cos\left(\frac{1}{3}\left[\arccos\left(\frac{R_\lambda}{\sqrt{-Q_\lambda^3}}\right)+2\pi\ell\right]\right)+\frac{2}{3}u, \quad \ell=0,1,2, \tag{3.2}$$

where

$$Q_\lambda = -\frac{1}{9}\left[u^2+3g(h+A(3u^2+v^2))\right], \quad R_\lambda = \frac{1}{54}\left[18ghu-2u^3-9Agu(3u^2+v^2))\right], \tag{3.3}$$

and

$$\mu^{(\ell)} = 2\sqrt{-Q_\mu}\cos\left(\frac{1}{3}\left[\arccos\left(\frac{R_\mu}{\sqrt{-Q_\mu^3}}\right)+2\pi\ell\right]\right)+\frac{2}{3}v, \quad \ell=0,1,2, \tag{3.4}$$

where

$$Q_\mu = -\frac{1}{9}\left[v^2+3g(h+A(u^2+3v^2))\right], \quad R_\mu = \frac{1}{54}\left[18ghv-2v^3-9Agv(u^2+3v^2))\right], \tag{3.5}$$

respectively.

One may show that both u and $\lambda^{(2)}$ in (3.2) are always between $\lambda^{(0)}$ and $\lambda^{(1)}$ and both v and $\mu^{(2)}$ in (3.4) are always between $\mu^{(0)}$ and $\mu^{(1)}$. We therefore will select the operator splitting time step based on the local speeds that correspond to the bottom topography propagation, that is, on $\lambda^{(2)}$ and $\mu^{(2)}$ to prevent excessive numerical diffusion to smear the computed (slowly moving) bottom structure.

3.1. Operator splitting. The 2-D operator splitting method is similar to the 1-D one. As before, we consider the hydrodynamic,

$$\begin{cases} \boldsymbol{U}_t+\boldsymbol{F}(\boldsymbol{U},B)_x+\boldsymbol{G}(\boldsymbol{U},B)_y=\boldsymbol{S}(\boldsymbol{U},B), \\ B_t=0 \end{cases} \tag{3.6}$$

with

$$\begin{gathered} \boldsymbol{U}=\begin{pmatrix} w \\ q \\ p \end{pmatrix}, \quad \boldsymbol{F}(\boldsymbol{U},B)=\begin{pmatrix} q+Au(u^2+v^2) \\ \dfrac{q^2}{w-B}+\dfrac{g}{2}(w-B)^2 \\ \dfrac{qp}{w-B} \end{pmatrix}, \\ \boldsymbol{G}(\boldsymbol{U},B)=\begin{pmatrix} p+Av(u^2+v^2) \\ \dfrac{qp}{w-B} \\ \dfrac{q^2}{w-B}+\dfrac{g}{2}(w-B)^2 \end{pmatrix}, \quad \boldsymbol{S}(\boldsymbol{U},B)=\begin{pmatrix} 0 \\ -g(w-B)B_x \\ -g(w-B)B_y \end{pmatrix}, \end{gathered} \tag{3.7}$$

and morphodynamic,

$$\begin{cases} \boldsymbol{U}_t=\boldsymbol{0}, \\ B_t+A\left(u(u^2+v^2)\right)_x+A\left(v(u^2+v^2)\right)_y=0. \end{cases} \tag{3.8}$$

subsystems. One step of the Strang operator splitting method is then still given by (2.10).

3.2. Semi-discretization of the hydrodynamic subsystem. We denote by $C_{j,k}:=[x_{j-\frac12},x_{j+\frac12}]\times[y_{k-\frac12},y_{k+\frac12}]$ the uniform Cartesian cells of size $\Delta x\Delta y$ centered at x_j and y_k. The computed solution, realized in terms of the cell averages $\overline{\boldsymbol{U}}_{j,k}\approx\frac{1}{\Delta x\Delta y}\iint_{C_{j,k}}\boldsymbol{U}(x,y,t)\,\mathrm{d}x\,\mathrm{d}y$ and point values $B_{j+\frac12,k+\frac12}\approx B(x_{j+\frac12},y_{k+\frac12})$, is assumed to be known at a given time t. The cell averages are evolved in time according to the well-balanced semi-discretization from [34]:

$$\frac{\mathrm{d}}{\mathrm{d}t}\overline{\boldsymbol{U}}_{j,k}=-\frac{\boldsymbol{H}^x_{j+\frac12,k}-\boldsymbol{H}^x_{j-\frac12,k}}{\Delta x}-\frac{\boldsymbol{H}^y_{j,k+\frac12}-\boldsymbol{H}^y_{j,k-\frac12}}{\Delta y}+\overline{\boldsymbol{S}}_{j,k},\tag{3.9}$$

where

$$\boldsymbol{H}^x_{j+\frac12,k}=\frac{a^+_{j+\frac12,k}\boldsymbol{F}^{\mathrm{E}}_{j,k}-a^-_{j+\frac12,k}\boldsymbol{F}^{\mathrm{W}}_{j+1,k}}{a^+_{j+\frac12,k}-a^-_{j+\frac12,k}}+\frac{a^+_{j+\frac12,k}a^-_{j+\frac12,k}}{a^+_{j+\frac12,k}-a^-_{j+\frac12,k}}\left[\boldsymbol{U}^{\mathrm{W}}_{j+1,k}-\boldsymbol{U}^{\mathrm{E}}_{j,k}\right]\tag{3.10}$$

and

$$\boldsymbol{H}^y_{j,k+\frac12}=\frac{a^+_{j,k+\frac12}\boldsymbol{G}^{\mathrm{N}}_{j,k}-a^-_{j,k+\frac12}\boldsymbol{G}^{\mathrm{S}}_{j,k+1}}{a^+_{j,k+\frac12}-a^-_{j,k+\frac12}}+\frac{a^+_{j,k+\frac12}a^-_{j,k+\frac12}}{a^+_{j,k+\frac12}-a^-_{j,k+\frac12}}\left[\boldsymbol{U}^{\mathrm{S}}_{j,k+1}-\boldsymbol{U}^{\mathrm{N}}_{j,k}\right]\tag{3.11}$$

are the central-upwind numerical fluxes in the x- and y-directions, respectively, and

$$\overline{\boldsymbol{S}}_{j,k}=\begin{pmatrix}0\\ -g\dfrac{h^{\mathrm{E}}_{j,k}+h^{\mathrm{W}}_{j,k}}{2}\cdot\dfrac{B_{j+\frac12,k+\frac12}+B_{j+\frac12,k-\frac12}-B_{j-\frac12,k+\frac12}-B_{j-\frac12,k-\frac12}}{2\Delta x}\\ -g\dfrac{h^{\mathrm{N}}_{j,k}+h^{\mathrm{S}}_{j,k}}{2}\cdot\dfrac{B_{j+\frac12,k+\frac12}+B_{j-\frac12,k+\frac12}-B_{j+\frac12,k-\frac12}-B_{j-\frac12,k-\frac12}}{2\Delta y}\end{pmatrix}$$

are the approximated cell averages of the geometric source term $\boldsymbol{S}$.

In (3.10) and (3.11),

$$\boldsymbol{F}^{\mathrm{E}}_{j,k}:=\boldsymbol{F}\left(\boldsymbol{U}^{\mathrm{E}}_{j,k},\frac{B_{j+\frac12,k+\frac12}+B_{j+\frac12,k-\frac12}}{2}\right),\quad \boldsymbol{F}^{\mathrm{W}}_{j,k}:=\boldsymbol{F}\left(\boldsymbol{U}^{\mathrm{W}}_{j,k},\frac{B_{j-\frac12,k+\frac12}+B_{j+\frac12,k-\frac12}}{2}\right),$$
$$\boldsymbol{G}^{\mathrm{N}}_{j,k}:=\boldsymbol{G}\left(\boldsymbol{U}^{\mathrm{N}}_{j,k},\frac{B_{j+\frac12,k+\frac12}+B_{j-\frac12,k+\frac12}}{2}\right),\quad \boldsymbol{G}^{\mathrm{S}}_{j,k}:=\boldsymbol{G}\left(\boldsymbol{U}^{\mathrm{S}}_{j,k},\frac{B_{j+\frac12,k-\frac12}+B_{j-\frac12,k-\frac12}}{2}\right),$$

where

$$\begin{aligned}&\boldsymbol{U}^{\mathrm{E}}_{j,k}=\overline{\boldsymbol{U}}_{j,k}+\frac{\Delta x}{2}(\boldsymbol{U}_x)_{j,k},\quad \boldsymbol{U}^{\mathrm{W}}_{j,k}=\overline{\boldsymbol{U}}_{j,k}-\frac{\Delta x}{2}(\boldsymbol{U}_x)_{j,k},\\ &\boldsymbol{U}^{\mathrm{N}}_{j,k}=\overline{\boldsymbol{U}}_{j,k}+\frac{\Delta y}{2}(\boldsymbol{U}_y)_{j,k},\quad \boldsymbol{U}^{\mathrm{S}}_{j,k}=\overline{\boldsymbol{U}}_{j,k}-\frac{\Delta y}{2}(\boldsymbol{U}_y)_{j,k}\end{aligned}\tag{3.12}$$

are the one-sided point values of $\boldsymbol{U}$ reconstructed inside the cell $C_{j,k}$ at the midpoints of the corresponding cell interfaces. As in the 1-D case, the slopes in (3.12) are computed using the generalized minmod limiter:

$$\begin{aligned}&(\boldsymbol{U}_x)_{j,k}=\mathrm{minmod}\left(\theta\frac{\overline{\boldsymbol{U}}_{j,k}-\overline{\boldsymbol{U}}_{j-1,k}}{\Delta x},\frac{\overline{\boldsymbol{U}}_{j+1,k}-\overline{\boldsymbol{U}}_{j-1,k}}{2\Delta x},\theta\frac{\overline{\boldsymbol{U}}_{j+1,k}-\overline{\boldsymbol{U}}_{j,k}}{\Delta x}\right),\\ &(\boldsymbol{U}_y)_{j,k}=\mathrm{minmod}\left(\theta\frac{\overline{\boldsymbol{U}}_{j,k}-\overline{\boldsymbol{U}}_{j,k-1}}{\Delta y},\frac{\overline{\boldsymbol{U}}_{j,k+1}-\overline{\boldsymbol{U}}_{j,k+1}}{2\Delta y},\theta\frac{\overline{\boldsymbol{U}}_{j,k+1}-\overline{\boldsymbol{U}}_{j,k}}{\Delta y}\right),\end{aligned}\tag{3.13}$$

where $\theta\in[1,2]$ and the minmod function is given by (2.15).

Finally, the local one-sided speeds of propagation in the x- and y-directions are obtained using the largest and smallest eigenvalues of the Jacobians of the system (3.1) in the x- and y-directions, respectively, and they are given by

$$\begin{aligned}
a^+_{j+\frac12,k}&=\max\Big\{\lambda^{(0),\mathrm{E}}_{j,k},\lambda^{(1),\mathrm{E}}_{j,k},\lambda^{(0),\mathrm{W}}_{j+1,k},\lambda^{(1),\mathrm{W}}_{j+1,k},0\Big\},\\
a^-_{j+\frac12,k}&=\min\Big\{\lambda^{(0),\mathrm{E}}_{j,k},\lambda^{(1),\mathrm{E}}_{j,k},\lambda^{(0),\mathrm{W}}_{j+1,k},\lambda^{(1),\mathrm{W}}_{j+1,k},0\Big\},\\
a^+_{j,k+\frac12}&=\max\Big\{\mu^{(0),\mathrm{N}}_{j,k},\mu^{(1),\mathrm{N}}_{j,k},\mu^{(0),\mathrm{S}}_{j,k+1},\mu^{(1),\mathrm{S}}_{j,k+1},0\Big\},\\
a^-_{j,k+\frac12}&=\min\Big\{\mu^{(0),\mathrm{N}}_{j,k},\mu^{(1),\mathrm{N}}_{j,k},\mu^{(0),\mathrm{S}}_{j,k+1},\mu^{(1),\mathrm{S}}_{j,k+1},0\Big\}.
\end{aligned}$$

Here, $\lambda^{(0),\mathrm{E}}_{j,k}$ and $\lambda^{(1),\mathrm{E}}_{j,k}$ are computed using (3.2), (3.3) with

$$h=h^{\mathrm{E}}_{j,k}=w^{\mathrm{E}}_{j,k}-\frac{B_{j+\frac12,k+\frac12}+B_{j+\frac12,k-\frac12}}{2},\quad u=\frac{q^{\mathrm{E}}_{j,k}}{h^{\mathrm{E}}_{j,k}},\quad v=\frac{p^{\mathrm{E}}_{j,k}}{h^{\mathrm{E}}_{j,k}},\tag{3.14}$$

and $\lambda^{(0),\mathrm{W}}_{j+1,k}$ and $\lambda^{(1),\mathrm{W}}_{j+1,k}$ are computed using (3.2), (3.3) with

$$h=h^{\mathrm{W}}_{j+1,k}=w^{\mathrm{W}}_{j+1,k}-\frac{B_{j+\frac12,k+\frac12}+B_{j+\frac12,k-\frac12}}{2},\quad u=\frac{q^{\mathrm{W}}_{j+1,k}}{h^{\mathrm{W}}_{j+1,k}},\quad v=\frac{p^{\mathrm{W}}_{j+1,k}}{h^{\mathrm{W}}_{j+1,k}}.\tag{3.15}$$

Similarly, $\mu^{(0),\mathrm{N}}_{j,k}$ and $\mu^{(1),\mathrm{N}}_{j,k}$ are computed using (3.4), (3.5) with

$$h=h^{\mathrm{N}}_{j,k}=w^{\mathrm{N}}_{j,k}-\frac{B_{j+\frac12,k+\frac12}+B_{j-\frac12,k+\frac12}}{2},\quad u=\frac{q^{\mathrm{N}}_{j,k}}{h^{\mathrm{N}}_{j,k}},\quad v=\frac{p^{\mathrm{N}}_{j,k}}{h^{\mathrm{N}}_{j,k}},\tag{3.16}$$

and $\mu^{(0),\mathrm{S}}_{j,k+1}$ and $\mu^{(1),\mathrm{S}}_{j,k+1}$ are computed using (3.4), (3.5) with

$$h=h^{\mathrm{S}}_{j,k+1}=w^{\mathrm{S}}_{j,k+1}-\frac{B_{j+\frac12,k+\frac12}+B_{j-\frac12,k+\frac12}}{2},\quad u=\frac{q^{\mathrm{S}}_{j,k+1}}{h^{\mathrm{S}}_{j,k+1}},\quad v=\frac{p^{\mathrm{S}}_{j,k+1}}{h^{\mathrm{S}}_{j,k+1}}.\tag{3.17}$$

3.3. Semi-discretization of the morphodynamic subsystem. In this section, we describe the semi-discrete central-upwind scheme for the system (3.8), which is discretized on a staggered grid with $C_{j+\frac12,k+\frac12}=[x_j,x_{j+1}]\times[y_k,y_{k+1}]$. As in the 1-D case, we first project the data, $\{\overline{\boldsymbol{U}}_{j,k}\}$, obtained at the hydrodynamic splitting step onto the staggered grid:

$$\begin{aligned}
\overline{\boldsymbol{U}}_{j+\frac12,k+\frac12}=&\frac{\overline{\boldsymbol{U}}_{j,k}+\overline{\boldsymbol{U}}_{j+1,k}+\overline{\boldsymbol{U}}_{j,k+1}+\overline{\boldsymbol{U}}_{j+1,k+1}}{4}\\
&-\frac{\Delta x}{16}\Big[(\boldsymbol{U}_x)_{j+1,k}-(\boldsymbol{U}_x)_{j,k}+(\boldsymbol{U}_x)_{j+1,k+1}-(\boldsymbol{U}_x)_{j,k+1}\Big],\\
&-\frac{\Delta y}{16}\Big[(\boldsymbol{U}_y)_{j,k+1}-(\boldsymbol{U}_y)_{j,k}+(\boldsymbol{U}_y)_{j+1,k+1}-(\boldsymbol{U}_y)_{j+1,k}\Big],
\end{aligned}$$

where the slopes $(\boldsymbol{U}_x)_j$ are computed using (3.13). $B_{j+\frac12,k+\frac12}$ are then evolved in time according to the following semi-discretization:

$$\frac{\mathrm{d}}{\mathrm{d}t}B_{j+\frac12,k+\frac12}=-\frac{H^x_{j+1,k+\frac12}-H^x_{j,k+\frac12}}{\Delta x}-\frac{H^y_{j+\frac12,k+1}-H^y_{j+\frac12,k}}{\Delta y},\tag{3.18}$$

where

$$H^x_{j,k+\frac12}=A\frac{b^+_{j,k+\frac12}F^{\rm E}_{j-\frac12,k+\frac12}-b^-_{j,k+\frac12}F^{\rm W}_{j+\frac12,k+\frac12}}{b^+_{j,k+\frac12}-b^-_{j,k+\frac12}}+\frac{b^+_{j,k+\frac12}b^-_{j,k+\frac12}}{b^+_{j,k+\frac12}-b^-_{j,k+\frac12}}\left[B^{\rm W}_{j+\frac12,k+\frac12}-B^{\rm E}_{j-\frac12,k+\frac12}\right] \tag{3.19}$$

and

$$H^y_{j+\frac12,k}=A\frac{b^+_{j+\frac12,k}G^{\rm N}_{j+\frac12,k-\frac12}-b^-_{j+\frac12,k}G^{\rm S}_{j+\frac12,k+\frac12}}{b^+_{j+\frac12,k}-b^-_{j+\frac12,k}}+\frac{b^+_{j+\frac12,k}b^-_{j+\frac12,k}}{b^+_{j+\frac12,k}-b^-_{j+\frac12,k}}\left[B^{\rm S}_{j+\frac12,k+\frac12}-B^{\rm N}_{j+\frac12,k-\frac12}\right] \tag{3.20}$$

are the central-upwind numerical fluxes.

In (3.19) and (3.20), we have used the following notation:

$$\begin{aligned}
F^{\rm E}_{j-\frac12,k+\frac12}&:=u^{\rm E}_{j-\frac12,k+\frac12}\left[\left(u^{\rm E}_{j-\frac12,k+\frac12}\right)^2+\left(v^{\rm E}_{j-\frac12,k+\frac12}\right)^2\right],\\
F^{\rm W}_{j+\frac12,k+\frac12}&:=u^{\rm W}_{j+\frac12,k+\frac12}\left[\left(u^{\rm W}_{j+\frac12,k+\frac12}\right)^2+\left(v^{\rm W}_{j+\frac12,k+\frac12}\right)^2\right],\\
G^{\rm N}_{j-\frac12,k+\frac12}&:=v^{\rm N}_{j+\frac12,k-\frac12}\left[\left(u^{\rm N}_{j+\frac12,k-\frac12}\right)^2+\left(v^{\rm N}_{j+\frac12,k-\frac12}\right)^2\right],\\
G^{\rm S}_{j+\frac12,k+\frac12}&:=v^{\rm S}_{j+\frac12,k+\frac12}\left[\left(u^{\rm S}_{j+\frac12,k+\frac12}\right)^2+\left(v^{\rm S}_{j+\frac12,k+\frac12}\right)^2\right].
\end{aligned} \tag{3.21}$$

The reconstructed point values of B in (3.19) and (3.20) are given by

$$B^{\rm E}_{j+\frac12,k+\frac12}=B_{j+\frac12,k+\frac12}+\frac{\Delta x}{2}(B_x)_{j+\frac12,k+\frac12},\quad B^{\rm W}_{j+\frac12,k+\frac12}=B_{j+\frac12,k+\frac12}-\frac{\Delta x}{2}(B_x)_{j+\frac12,k+\frac12},$$
$$B^{\rm N}_{j+\frac12,k+\frac12}=B_{j+\frac12,k+\frac12}+\frac{\Delta y}{2}(B_y)_{j+\frac12,k+\frac12},\quad B^{\rm S}_{j+\frac12,k+\frac12}=B_{j+\frac12,k+\frac12}-\frac{\Delta y}{2}(B_y)_{j+\frac12,k+\frac12},$$

where the slopes are, as before, computed using the generalized minmod limiter:

$$\begin{aligned}
(B_x)_{j+\frac12,k+\frac12}=\text{minmod}\Bigg(&\theta\frac{B_{j+\frac12,k+\frac12}-B_{j-\frac12,k+\frac12}}{\Delta x},\frac{B_{j+\frac32,k+\frac12}-B_{j-\frac12,k+\frac12}}{2\Delta x},\\
&\theta\frac{B_{j+\frac32,k+\frac12}-B_{j+\frac12,k+\frac12}}{\Delta x}\Bigg),\\
(B_y)_{j+\frac12,k+\frac12}=\text{minmod}\Bigg(&\theta\frac{B_{j+\frac12,k+\frac12}-B_{j+\frac12,k-\frac12}}{\Delta y},\frac{B_{j+\frac12,k+\frac32}-B_{j+\frac12,k-\frac12}}{2\Delta y},\\
&\theta\frac{B_{j+\frac12,k+\frac32}-B_{j+\frac12,k+\frac12}}{\Delta x}\Bigg),
\end{aligned}$$

and the minmod function is defined by (2.15). The reconstructed point values $w^i_{j+\frac12,k+\frac12}$ and $q^i_{j+\frac12,k+\frac12}$, $i\in\{\rm E,W,N,S\}$ are obtained in a similar manner and then used to calculate the corresponding values of the velocities, which are needed in (3.19)–(3.21):

$$u^i_{j+\frac12,k+\frac12}=\frac{q^i_{j+\frac12,k+\frac12}}{w^i_{j+\frac12,k+\frac12}-B^i_{j+\frac12,k+\frac12}},\quad v^i_{j+\frac12,k+\frac12}=\frac{p^i_{j+\frac12,k+\frac12}}{w^i_{j+\frac12,k+\frac12}-B^i_{j+\frac12,k+\frac12}}.$$

Finally, $b^{\pm}_{j,k+\frac{1}{2}}$ and $b^{\pm}_{j+\frac{1}{2},k}$ are local one-sided speeds of propagation in the x- and y-directions, respectively, are given by

$$b^{+}_{j,k+\frac{1}{2}}=\max\left\{\lambda^{(2),\mathrm{E}}_{j-\frac{1}{2},k+\frac{1}{2}},\lambda^{(2),\mathrm{W}}_{j+\frac{1}{2},k+\frac{1}{2}},0\right\},\quad b^{-}_{j,k+\frac{1}{2}}=\min\left\{\lambda^{(2),\mathrm{E}}_{j-\frac{1}{2},k+\frac{1}{2}},\lambda^{(2),\mathrm{W}}_{j+\frac{1}{2},k+\frac{1}{2}},0\right\},$$
$$b^{+}_{j+\frac{1}{2},k}=\max\left\{\mu^{(2),\mathrm{N}}_{j+\frac{1}{2},k-\frac{1}{2}},\mu^{(2),\mathrm{S}}_{j+\frac{1}{2},k+\frac{1}{2}},0\right\},\quad b^{-}_{j+\frac{1}{2},k}=\min\left\{\mu^{(2),\mathrm{N}}_{j+\frac{1}{2},k-\frac{1}{2}},\mu^{(2),\mathrm{S}}_{j+\frac{1}{2},k+\frac{1}{2}},0\right\},$$

Here, $\lambda^{(2),\mathrm{E}}_{j-\frac{1}{2},k+\frac{1}{2}}$ is computed using (3.2), (3.3) with

$$h=h^{\mathrm{E}}_{j-\frac{1}{2},k+\frac{1}{2}}=w^{\mathrm{E}}_{j-\frac{1}{2},k+\frac{1}{2}}-B^{\mathrm{E}}_{j-\frac{1}{2},k+\frac{1}{2}},\quad u=\frac{q^{\mathrm{E}}_{j-\frac{1}{2},k+\frac{1}{2}}}{h^{\mathrm{E}}_{j-\frac{1}{2},k+\frac{1}{2}}},\quad v=\frac{p^{\mathrm{E}}_{j-\frac{1}{2},k+\frac{1}{2}}}{h^{\mathrm{E}}_{j-\frac{1}{2},k+\frac{1}{2}}},$$

and $\lambda^{(2),\mathrm{W}}_{j+\frac{1}{2},k+\frac{1}{2}}$ is computed using (3.2), (3.3) with

$$h=h^{\mathrm{W}}_{j+\frac{1}{2},k+\frac{1}{2}}=w^{\mathrm{W}}_{j+\frac{1}{2},k+\frac{1}{2}}-B^{\mathrm{W}}_{j+\frac{1}{2},k+\frac{1}{2}},\quad u=\frac{q^{\mathrm{W}}_{j+\frac{1}{2},k+\frac{1}{2}}}{h^{\mathrm{W}}_{j+\frac{1}{2},k+\frac{1}{2}}},\quad v=\frac{p^{\mathrm{W}}_{j+\frac{1}{2},k+\frac{1}{2}}}{h^{\mathrm{W}}_{j+\frac{1}{2},k+\frac{1}{2}}}.$$

Similarly, $\mu^{(2),\mathrm{N}}_{j+\frac{1}{2},k-\frac{1}{2}}$ is computed using (3.4), (3.5) with

$$h=h^{\mathrm{N}}_{j+\frac{1}{2},k-\frac{1}{2}}=w^{\mathrm{N}}_{j+\frac{1}{2},k-\frac{1}{2}}-B^{\mathrm{N}}_{j+\frac{1}{2},k-\frac{1}{2}},\quad u=\frac{q^{\mathrm{N}}_{j+\frac{1}{2},k-\frac{1}{2}}}{h^{\mathrm{N}}_{j+\frac{1}{2},k-\frac{1}{2}}},\quad v=\frac{p^{\mathrm{N}}_{j+\frac{1}{2},k-\frac{1}{2}}}{h^{\mathrm{N}}_{j+\frac{1}{2},k-\frac{1}{2}}},$$

and $\mu^{(2),\mathrm{S}}_{j+\frac{1}{2},k+\frac{1}{2}}$ is computed using (3.4), (3.5) with

$$h=h^{\mathrm{S}}_{j+\frac{1}{2},k+\frac{1}{2}}=w^{\mathrm{S}}_{j+\frac{1}{2},k+\frac{1}{2}}-B^{\mathrm{S}}_{j+\frac{1}{2},k+\frac{1}{2}},\quad u=\frac{q^{\mathrm{S}}_{j+\frac{1}{2},k+\frac{1}{2}}}{h^{\mathrm{S}}_{j+\frac{1}{2},k+\frac{1}{2}}},\quad v=\frac{p^{\mathrm{S}}_{j+\frac{1}{2},k+\frac{1}{2}}}{h^{\mathrm{S}}_{j+\frac{1}{2},k+\frac{1}{2}}}.$$

3.4. Summary of the algorithm. In this section, we summarize one time step of the 2-D splitting method assuming that at a certain time level t the computed quantities $\{\overline{w}_{j,k}\}$, $\{\overline{q}_{j,k}\}$, $\{\overline{p}_{j,k}\}$ and $\left\{B_{j+\frac{1}{2},k+\frac{1}{2}}\right\}$ are available.

Step 1. Compute $w^{i}_{j,k}$, $q^{i}_{j,k}$ and $p^{i}_{j,k}$, $i\in\{\mathrm{E},\mathrm{W},\mathrm{N},\mathrm{S}\}$ using (3.12), (3.13).

Step 2. Compute

$$b^{x}_{\max}:=\max_{j,k}\left\{\max\left\{\left|\lambda^{(2),\mathrm{E}}_{j,k}\right|,\left|\lambda^{(2),\mathrm{W}}_{j+1,k}\right|\right\}\right\}\quad\text{and}\quad b^{y}_{\max}:=\max_{j,k}\left\{\max\left\{\left|\mu^{(2),\mathrm{N}}_{j,k}\right|,\left|\mu^{(2),\mathrm{S}}_{j,k+1}\right|\right\}\right\},$$

where $\lambda^{(2),\mathrm{E}}_{j,k}$ are computed using (3.2), (3.3) with h, u and v given by (3.14), $\lambda^{(2),\mathrm{W}}_{j+1,k}$ are computed using (3.2), (3.3) with h, u and v given by (3.15), $\mu^{(2),\mathrm{N}}_{j,k}$ are computed using (3.4), (3.5) with h, u and v given by (3.16), and $\mu^{(2),\mathrm{S}}_{j,k+1}$ are computed using (3.4), (3.5) with h, u and v given by (3.17).

Step 3. Choose the splitting time step Δt based on the CFL-type condition for the morphodynamic subsystem:

$$\Delta t=\mathcal{K}\min\left\{\frac{\Delta x}{b^{x}_{\max}},\frac{\Delta y}{b^{y}_{\max}}\right\},\tag{3.22}$$

where $\mathcal{K}$ is, as before, a CFL constant.

Step 4. Evolve $\{\overline{\boldsymbol{U}}_{j,k}\}$ by numerically solving the ODE system (3.9) from time level t to $t+\Delta t/2$ using the three-stage third-order SSP Runge-Kutta method with the time step Δt_H being constrained by the following CFL-like condition:

$$\Delta t_H \le \mathcal{K}\min\left\{\frac{\Delta x}{a^x_{\max}},\frac{\Delta y}{a^y_{\max}}\right\}, \tag{3.23}$$

where

$$a^x_{\max}:=\max_{j,k}\left\{\max\left\{a^+_{j+\frac12,k},-a^-_{j+\frac12,k}\right\}\right\} \quad \text{and} \quad a^y_{\max}:=\max_{j,k}\left\{\max\left\{a^+_{j,k+\frac12},-a^-_{j,k+\frac12}\right\}\right\}. \tag{3.24}$$

Denote the obtained solution by $\{\overline{\boldsymbol{U}}^*_{j,k}\}$.

Step 5. Evolve $\{B_{j+\frac12,k+\frac12}\}$ by numerically solving the ODE system (3.18) from time level t to $t+\Delta t$ using the three-stage third-order SSP Runge-Kutta method.

Step 6. Evolve $\{\overline{\boldsymbol{U}}^*_{j,k}\}$ by numerically solving the ODE system (3.9) from time level $t+\Delta t/2$ to $t+\Delta t$ with the time step Δt_H being constrained by (3.23), (3.24).

Step 7. Set $t=t+\Delta t$ and go to Step 1.

4. Numerical examples

In this section, we present six numerical examples. In all of the examples, the water-sediment interaction model was considered with the gravitational acceleration $g=9.8$ and free flow boundary conditions on all sides of the computational domain. The minmod limiter was computed with $\theta=1.3$ and the CFL constant was taken $\mathcal{K}=0.475$.

We note that one can choose the size of the splitting step Δt according to the stricter CFL conditions (2.19) and (3.23) instead of (2.18) and (3.22), respectively. This would lead to smaller splitting time steps and thus a somewhat smaller splitting error, but it would increase the CPU times by a factor of about 3. We observed, however, that the use of smaller splitting time steps did not lead to any significant improvement in the quality of the obtained numerical solutions since the other discretization errors seem to dominate the operator splitting one. Therefore, we only report the results obtained according to the algorithms presented in §2.4 and §3.4.

Example 1—Accuracy test. In this example, taken from [4], we consider a 1-D channel on the interval $[-10,10]$, with $A=0.5$ in (2.2), the final time $t=0.2$, and initial conditions given by:

$$h(x,0)=2-0.1e^{-x^2},\quad q(x,0)\equiv 0,\quad B(x,0)=0.1-0.01e^{-x^2}.$$

Since the exact solution is unknown, we compare the computed solutions with a reference one obtained using a very fine mesh consisting of $N=6400$ uniform cells. The solutions computed using $N=50$, 100, 200 and 400 uniform cells are plotted in Figure 4.1. The L^1- and L^2-errors together with the corresponding experimental convergence rates for both h, q and B are presented in Table 4.1 and 4.2. As one can see, the proposed scheme achieves the expected second order of convergence.

Example 2—Weak water-sediment interaction. In this problem taken from [10], the interaction between the water and moving bottom topography is weak. This is modeled by taking the constant A in the Exner Equation (2.2) to be relatively small,

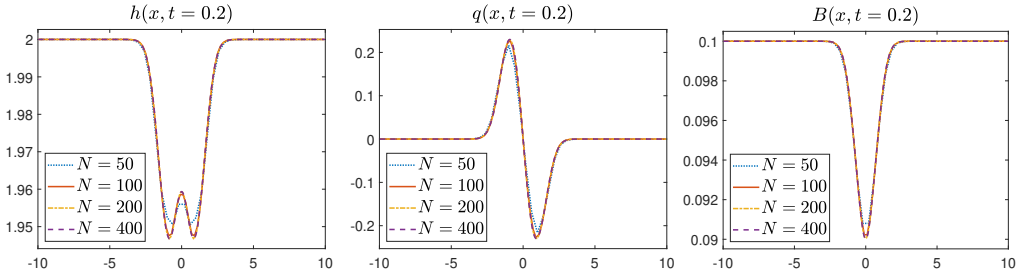

FIG. 4.1. *Example 1: Solution (h, q and B) computed on four different grids.*

N	Error in h	rate	Error in q	rate	Error in B	rate
50	9.20E-3	–	5.91E-2	–	5.86E-4	–
100	2.20E-3	2.06	1.29E-2	2.19	1.65E-4	1.82
200	5.45E-4	2.16	2.74E-3	2.24	4.35E-5	1.92
400	1.36E-4	2.01	6.06E-4	2.17	1.07E-5	2.02

TABLE 4.1. *Example 1: L^1-errors and corresponding experimental convergence rates.*

N	Error in h	rate	Error in q	rate	Error in B	rate
50	4.98E-3	–	3.27E-2	–	3.62E-4	–
100	1.00E-3	2.31	6.89E-2	2.24	9.83E-5	1.88
200	2.52E-4	1.99	1.35E-3	2.35	2.53E-5	1.96
400	6.48E-4	1.95	2.96E-4	2.19	6.27E-6	2.01

TABLE 4.2. *Example 1: L^2-errors and corresponding experimental convergence rates.*

namely, $A=0.005$. The initial data,

$$\begin{aligned} &q(x,0)\equiv 0.5, \quad B(x,0)=0.1(1+e^{-(x-5)^2}),\\ &\frac{q^2(x,0)}{2h^2(x,0)}+g[h(x,0)+B(x,0)]\equiv 6.386, \end{aligned} \tag{4.1}$$

correspond to a subcritical moving-water steady state for the SV system (2.7), (2.8). We note that $h(x,0)$ can be obtained by solving the third equation in (4.1), which is a cubic equation and details on its exact solution can be found in [37]; also see [28].

We compute the solution until the final time $t=10$ in the interval $[0,10]$ using $N=400$ uniform cells. The obtained results, presented in Figure 4.2 (left), are in good agreement with the reference solution computed on a much finer mesh with $N=4000$ uniform cells as well as with the results reported in [10]. This demonstrates that our splitting method is capable of handling cases with weak water-sediment interactions.

It is instructive to compare the values of $a^{\pm}$ with the largest/smallest eigenvalues of the SV system (2.7), (2.8), that is, $u\pm\sqrt{gh}$. As the water-sediment interaction is quite weak in this example, one expects these quantities to be close to each other. Indeed, this is true as one can see from Figure 4.2 (right). We also plot there the value of $\lambda^{(2)}$, which is, as expected, very small in this case.

Example 3—Strong water-sediment interaction. In this problem, also taken from [10], we consider system (2.3), (2.2) subject to the same initial condition (4.1) as

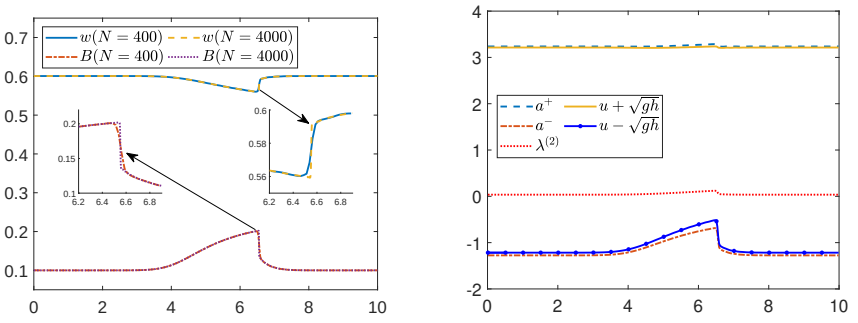

FIG. 4.2. *Example 2: Computed water surface w and bottom topography B (left) and the local speeds of both the coupled SV-Exner system (2.3), (2.2) and classical SV system (2.7), (2.8).*

in Example 2, but with stronger sediment-water interaction modeled by choosing larger $A=0.07$.

We implement the proposed splitting approach and compute the numerical solution until the final time $t=2.1$ in the interval $[0,10]$ using $N=400$ uniform cells. The obtained results, plotted in Figure 4.3 (left), agree well with the reference solution computed on a much finer mesh with $N=4000$ uniform cells as well as with the results reported in [10]. This clearly demonstrates that our method is capable of handling strong water-sediment interactions without producing spurious oscillations.

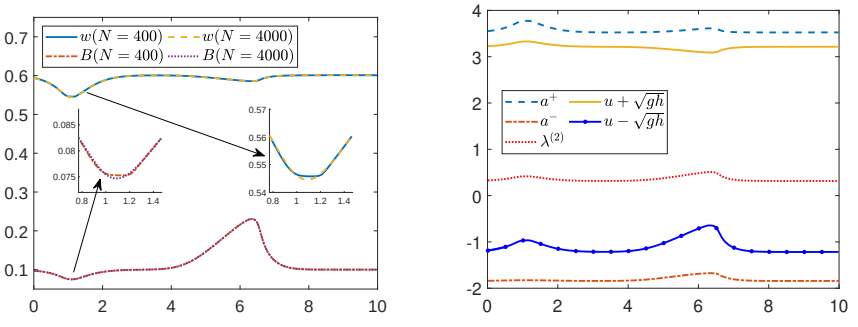

FIG. 4.3. *Example 3: Computed water surface w and bottom topography B (left) and the local speeds of both the coupled SV-Exner system (2.3), (2.2) and classical SV system (2.7), (2.8).*

The main difference between the experiments with $A=0.005$ (Example 2) and $A=0.07$ is that in the latter case, the local speeds of propagation $a^{\pm}$ are far from the eigenvalues of the SV system (2.7), (2.8), that is, $u\pm\sqrt{gh}$, as illustrated in Figure 4.3 (right). Therefore, using the correct bounds for the local propagation speeds is essential for obtaining highly accurate and stable results since in the stronger interaction case, the numerical solution is more likely to produce oscillations; see [10, 22] for details.

Example 4—Sediment mound with weak water-sediment interaction. In this problem, taken from [22, 23], we numerically solve the system (2.3), (2.2) with $A=1/600$ in the computational domain $[0,1000]$ and subject to the initial data given

by

$$w(x,0)\equiv 10,\quad q(x,0)\equiv 10,\quad B(x,0)=\begin{cases}\sin^2\Big(\dfrac{\pi(x-300)}{200}\Big), & 300\le x\le 500,\\ 0, & \text{otherwise.}\end{cases}$$

We compute the numerical solution until the final time $t=238079$ seconds on a series of uniform grids with $N=100$, 200 and 400 cells and compare the obtained results with the reference solution calculated analytically using the method of characteristics in [22]. As shown in Figure 4.4, the computed B converges to the reference one as N increases.

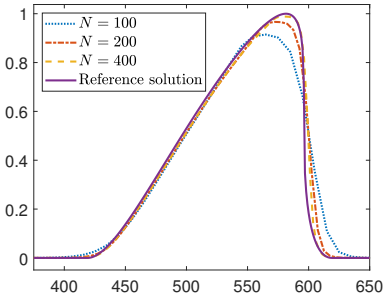

FIG. 4.4. *Example 4: Bottom topography B computed on a series of grids.*

Example 5—Discontinuous bottom topography. In this example, taken from [22], we consider the same setting as in Example 4 with the only difference in the description of the bottom topography, which now contains a jump:

$$B(x,0)=\begin{cases}1, & x\le 300,\\ 0, & \text{otherwise.}\end{cases}$$

This discontinuity propagates down the channel and in Figure 4.5, we plot B computed on a uniform mesh with 200 cells at the final time $t=250$ hours (900000 seconds). As one can observe, the propagating wave is sharply resolved and the proposed numerical method clearly outperforms the ones studied in [22].

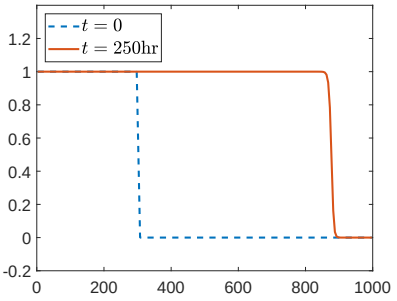

FIG. 4.5. *Example 5: Bottom topography B at two different times.*

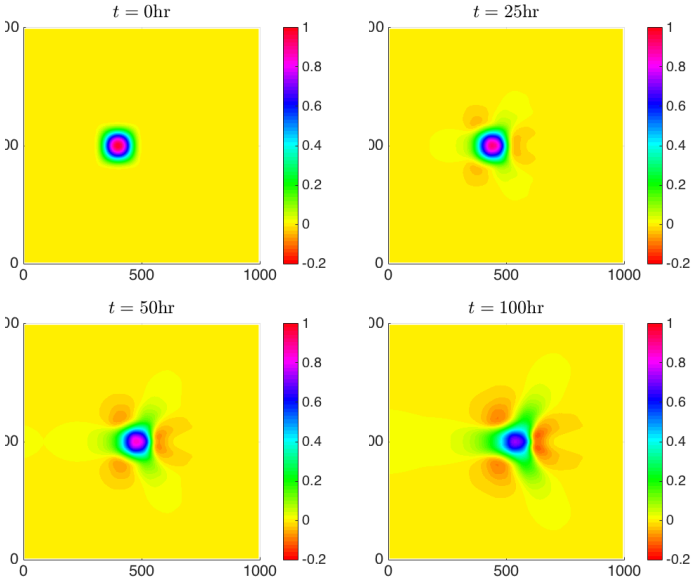

FIG. 4.6. *Example 6: Bottom topography B at four different times.*

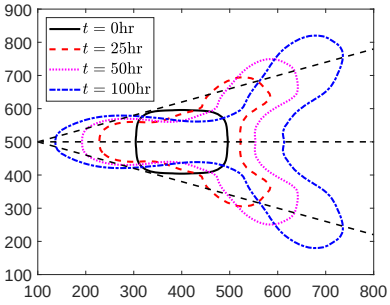

FIG. 4.7. *Example 6: Estimation of the spreading angle.*

Example 6—Evolution of conical dune. In the last example, we test the proposed 2-D scheme on a conical sand dune problem, which is a slightly modified version of the problems studied in [2, 5, 12, 22, 24]. We numerically solve the system (3.1) with $A=1/600$ in the computational domain $[0,1000]\times[0,1000]$ and subject to the initial data given by

$$w(x,y,0)\equiv 10,\quad q(x,y,0)\equiv 10,\quad p(x,y,0)\equiv 0,$$

$$B(x,y,0)=\begin{cases}\sin^2\left(\dfrac{\pi(x-300)}{200}\right)\sin^2\left(\dfrac{\pi(y-400)}{200}\right), & (x,y)\in[300,500]\times[400,600],\\ 0, & \text{otherwise.}\end{cases}$$

We compute the numerical solution until the final time $t=100$ hours (360000 seconds) on a uniform mesh with 100×100 cells. As time is evolved, the conical dune gradually spreads out into a star shaped pattern as demonstrated in Figure 4.6, where we plot the bottom topography B at times $t=0$, 25, 50 and 100 hours. According to the analysis

in [12], the angle of spread has to be approximately 21.79 degrees from the line of symmetry $y=500$. In Figure 4.7, we plot the level curves at the base of the dune at times $t=0$, 25, 50 and 100 hours. The angles between the dashed lines are 21.79 degrees and one can see that the spread is mostly contained between the lines, and the results are similar to those reported in [2,5,22,24].

5. Conclusion

In this paper, we have studied the shallow water system with time-dependent bottom topography. We have considered the simplest case, in which the shallow water waves are modeled by the Saint-Venant system and the bottom topography movement is governed by the Exner equation. The resulting system is hyperbolic and its Jacobian matrices typically contain both large and small eigenvalues. The largest eigenvalues determine the speed of the fast surface waves, while the smallest eigenvalue reflects the (slow) speed of the bottom topography propagation. Therefore, if the entire system is solved using an explicit finite-volume method, the time steps, which are inversely proportional to the maximum of the spectral radius of the Jacobians over the entire computational domain, would be too small. This may prevent high resolution of the bottom topography waves, especially when they contain sharp (discontinuous) fronts. In order to tackle this difficulty, we have developed an operator splitting approach, which allows one to take large time steps in the bottom evolution stages, while keeping the small CFL-controlled time steps in the hydrodynamics stages. The time evolution within each of the stages is carried out using the central-upwind scheme, which naturally leads to the following staggered approach: while the hydrodynamics quantities are sampled at the centers of each computational cell, the bottom topography data are prescribed at the corners.

We have demonstrated high accuracy and robustness of the proposed numerical method on a number of numerical experiments. In the future works, we plan to extend our method to more realistic water-sediment interaction models, for example, to those proposed and studied in [6,7,15–17,36,43,48].

Acknowledgments. The work of A. Chertock was supported in part by NSF grant DMS-1818684. The work of A. Kurganov was supported in part by NSFC grant 11771201 and by the fund of the Guangdong Provincial Key Laboratory of Computational Science and Material Design (No. 2019B030301001).

REFERENCES

[1] E. Audusse, F. Bouchut, M.-O. Bristeau, R. Klein, and B. Perthame, *A fast and stable well-balanced scheme with hydrostatic reconstruction for shallow water flows*, SIAM J. Sci. Comput., 25:2050–2065, 2004. 1

[2] F. Benkhaldoun, S. Sahmim, and M. Seaïd, *A two-dimensional finite volume morphodynamic model on unstructured triangular grids*, Int. J. Numer. Methods Fluids, 63(11):1296–1327, 2010. 1, 4

[3] A. Bollermann, S. Noelle, and M. Lukáčová-Medviďová, *Finite volume evolution Galerkin methods for the shallow water equations with dry beds*, Commun. Comput. Phys., 10(2):371–404, 2011. 1

[4] M.J. Castro Díaz, E.D. Fernández-Nieto, and A.M. Ferreiro, *Sediment transport models in shallow water equations and numerical approach by high order finite volume methods*, Comput. Fluids, 37(3):299–316, 2008. 4

[5] M.J. Castro Díaz, E.D. Fernández-Nieto, A.M. Ferreiro, and C. Parés, *Two-dimensional sediment transport models in shallow water equations. A second order finite volume approach on unstructured meshes*, Comput. Meth. Appl. Mech. Engrg., 198(33-36):2520–2538, 2009. 1, 4

[6] M.J. Castro Díaz, E.D. Fernández-Nieto, T. Morales de Luna, G. Narbona-Reina, and M. de la

Asunción, *Bed load sediment transport in shallow flows: models and numerics, an overview*, preprint. 5

[7] F. Charru, *Selection of the ripple length on a granular bed sheared by a liquid flow*, Phys. Fluids, 18(12):121508, 2006. 5

[8] A. Chertock and A. Kurganov, *On splitting-based numerical methods for convection-diffusion equations*, in Numerical Methods for Balance Laws, Quad. Mat., Dept. Math., Seconda Univ. Napoli, Caserta, 24:303–343, 2009. 1

[9] A. Chertock, A. Kurganov, and G. Petrova, *Fast explicit operator splitting method for convection-diffusion equations*, Int. J. Numer. Methods Fluids, 59:309–332, 2009. 1

[10] S. Cordier, M.H. Le, and T. Morales de Luna, *Bedload transport in shallow water models: Why splitting (may) fail, how hyperbolicity (can) help*, Adv. Water Resour., 34(8):980–989, 2011. 4, 4, 4, 4

[11] A.J.C. de Saint-Venant, *Thèorie du mouvement non-permanent des eaux, avec application aux crues des rivière at à l'introduction des marèes dans leur lit*, C.R. Acad. Sci. Paris, 73:147–154, 237–240, 1871. 1

[12] H.J. de Vriend, *2DH mathematical modelling of morphological evolutions in shallow water*, Coast. Eng., 11(1):1–27, 1987. 4

[13] A.I. Delis and I. Papoglou, *Relaxation approximation to bed-load sediment transport*, J. Comput. Appl. Math., 213(2):521–546, 2008. 1

[14] F.M. Exner, *Zur Physik der Dünen*, Hölder, 1920. 1

[15] E.D. Fernández-Nieto, C. Lucas, T. Morales de Luna, and S. Cordier, *On the influence of the thickness of the sediment moving layer in the definition of the bedload transport formula in Exner systems*, Comput. Fluids, 91:87–106, 2014. 5

[16] E.D. Fernández-Nieto, T. Morales de Luna, G. Narbona-Reina, and J.D. Zabsonré, *Formal deduction of the Saint-Venant-Exner model including arbitrarily sloping sediment beds and associated energy*, ESAIM Math. Model. Numer. Anal., 51(1):115–145, 2017. 5

[17] A.C. Fowler, N. Kopteva, and C. Oakley, *The formation of river channels*, SIAM J. Appl. Math., 67(4):1016–1040, 2007. 5

[18] S. Gottlieb, D. Ketcheson, and C.-W. Shu, *Strong Stability Preserving Runge-Kutta and Multistep Time Discretizations*, World Scientific Publishing Co. Pte. Ltd., Hackensack, NJ, 188, 2011. 2.2

[19] S. Gottlieb, C.-W. Shu, and E. Tadmor, *Strong stability-preserving high-order time discretization methods*, SIAM Rev., 43(1):89–112, 2001. 2.2

[20] A.J. Grass, *Sediment Transport by Waves and Currents*, University College, London, Dept. of Civil Engineering, 1981. 1

[21] P. Heinrich, *Nonlinear water waves generated by submarine and areal landslides*, J. Waterway Port Coast. Ocean Eng., 118:249–266, 1992. 1

[22] J. Hudson, *Numerical techniques for morphodynamic modelling*, PhD thesis, University of Reading, 2001. 4, 4, 4, 4

[23] J. Hudson and P.K. Sweby, *Formulations for numerically approximating hyperbolic systems governing sediment transport*, J. Sci. Comput., 19(1-3):225–252, 2003. 1, 4

[24] J. Hudson and P.K. Sweby, *A high-resolution scheme for the equations governing 2D bed-load sediment transport*, Int. J. Numer. Methods Fluids, 47(10-11):1085–1091, 2005. 1, 4

[25] H. Jia and K. Li, *A third accurate operator splitting method*, Math. Comput. Modelling, 53(1-2):387–396, 2011. 1, 2.1

[26] G.-S. Jiang, D. Levy, C.-T. Lin, S. Osher, and E. Tadmor, *High-resolution nonoscillatory central schemes with nonstaggered grids for hyperbolic conservation laws*, SIAM J. Numer. Anal., 35(6):2147–2168, 1998. 2.3

[27] S. Jin, *A steady-state capturing method for hyperbolic systems with geometrical source terms*, M2AN Math. Model. Numer. Anal., 35(4):631–645, 2001. 1

[28] C. Klingenberg, A. Kurganov, Y. Liu, and M. Zenk, *Moving-water equilibria preserving HLL-type schemes for the shallow water equations*, Commun. Math. Res., 36:247–271,2020. 4

[29] A. Kurganov, *Central schemes: a powerful black-box solver for nonlinear hyperbolic PDEs*, in R. Abgrall and C.-W. Shu (eds.), Handbook of Numerical Methods for Hyperbolic Problems, Elsevier/North-Holland, Amsterdam, 17:525–548, 2016. 2.4

[30] A. Kurganov, *Finite-volume schemes for shallow-water equations*, Acta Numer., 27:289–351, 2018. 1, 2.4

[31] A. Kurganov and D. Levy, *Central-upwind schemes for the Saint-Venant system*, M2AN Math. Model. Numer. Anal., 36(3):397–425, 2002. 1, 2

[32] A. Kurganov and C.-T. Lin, *On the reduction of numerical dissipation in central-upwind schemes*, Commun. Comput. Phys., 2(1):141–163, 2007. 1

[33] A. Kurganov, S. Noelle, and G. Petrova, *Semidiscrete central-upwind schemes for hyperbolic*

conservation laws and Hamilton-Jacobi equations, SIAM J. Sci. Comput., 23(3):707–740, 2001. 1

[34] A. Kurganov and G. Petrova, *A second-order well-balanced positivity preserving central-upwind scheme for the Saint-Venant system*, Commun. Math. Sci., 5(1):133–160, 2007. 1, 2, 2.2, 3.2

[35] A. Kurganov and E. Tadmor, *New high-resolution central schemes for nonlinear conservation laws and convection-diffusion equations*, J. Comput. Phys., 160(1):241–282, 2000. 1

[36] P.-Y. Lagrée, L. Staron, and S. Popinet, *The granular column collapse as a continuum: validity of a two-dimensional Navier-Stokes model with a $\mu(I)$-rheology*, J. Fluid Mech., 686:378–408, 2011. 5

[37] W.D. Lambert, *A generalized trigonometric solution of the cubic equation*, Amer. Math. Monthly, 13(4):73–76, 1906. 4

[38] J. Lee and B. Fornberg, *A split step approach for the 3-D Maxwell's equations*, J. Comput. Appl. Math., 158(2):485–505, 2003. 2.1

[39] R.J. LeVeque, *Balancing source terms and flux gradients in high-resolution Godunov methods: the quasi-steady wave-propagation algorithm*, J. Comput. Phys., 146(1):346–365, 1998. 1

[40] S. Li and C.J. Duffy, *Fully coupled approach to modeling shallow water flow, sediment transport, and bed evolution in rivers*, Water Resour. Res., 47(3):1–20, 2011. 1

[41] K.-A. Lie and S. Noelle, *On the artificial compression method for second-order nonoscillatory central difference schemes for systems of conservation laws*, SIAM J. Sci. Comput., 24(4):1157–1174, 2003. 2.2

[42] G.I. Marchuk, *Splitting and alternating direction methods*, in P.G. Ciarlet and J.L. Lions (eds.), Handbook of Numerical Analysis, Vol. I, North-Holland, Amsterdam, 197–462, 1990. 1

[43] T. Morales de Luna, M.J. Castro Díaz, and C. Parés Madroñal, *A duality method for sediment transport based on a modified Meyer-Peter & Müller model*, J. Sci. Comput., 48(1-3):258–273, 2011. 5

[44] T. Morales de Luna, M.J. Castro Díaz, C. Parés Madroñal, and E.D. Fernández Nieto, *On a shallow water model for the simulation of turbidity currents*, Commun. Comput. Phys., 6(4):848–882, 2009. 1

[45] J. Murillo and P. García-Navarro, *An Exner-based coupled model for two-dimensional transient flow over erodible bed*, J. Comput. Phys., 229(23):8704–8732, 2010. 1

[46] H. Nessyahu and E. Tadmor, *Nonoscillatory central differencing for hyperbolic conservation laws*, J. Comput. Phys., 87(2):408–463, 1990. 2.2

[47] R.W.D. Nickalls, *A new approach to solving the cubic: Cardans solution revealed*, Math. Gaz., 77(480):354–359, 1993. 2

[48] P. Nielsen, *Coastal Bottom Boundary Layers and Sediment Transport*, World Scientific, 4, 1992. 5

[49] S. Noelle, Y. Xing, and C.-W. Shu, *High-order well-balanced finite volume WENO schemes for shallow water equation with moving water*, J. Comput. Phys., 226(1):29–58, 2007. 1

[50] D. Pritchard and A.J. Hogg, *On sediment transport under dam-break flow*, J. Fluid Mech., 473:265–274, 2002. 1

[51] G. Simpson and S. Castelltort, *Coupled model of surface water flow, sediment transport and morphological evolution*, Comput. Geosci., 32(10):1600–1614, 2006. 1

[52] G. Strang, *On the construction and comparison of difference schemes*, SIAM J. Numer. Anal., 5:506–517, 1968. 1

[53] M. Suzuki, *General theory of fractal path integrals with applications to many-body theories and statistical physics*, J. Math. Phys., 32(2):400–407, 1991. 2.1

[54] P.K. Sweby, *High resolution schemes using flux limiters for hyperbolic conservation laws*, SIAM J. Numer. Anal., 21(5):995–1011, 1984. 2.2

[55] P.N. Vabishchevich, *Additive Operator-Difference Schemes*, De Gruyter, Berlin, 2014. 1

[56] B. van Leer, *Towards the ultimate conservative difference scheme. V. A second-order sequel to Godunov's method*, J. Comput. Phys., 32(1):101–136, 1979. 2.2

[57] P. Watts, *Tsunami features of solid block underwater landslides*, J. Waterway Port Coast. Ocean Eng., 126(3):144–152, 2000. 1

[58] J. Xia, B. Lin, R.A. Falconer, and G. Wang, *Modelling dam-break flows over mobile beds using a 2D coupled approach*, Adv. Water Resour., 33(2):171–183, 2010. 1

[59] Y. Xing and C.-W. Shu, *A new approach of high order well-balanced finite volume WENO schemes and discontinuous Galerkin methods for a class of hyperbolic systems with source terms*, Commun. Comput. Phys., 1:100–134, 2006. 1

[60] H. Yoshida, *Construction of higher order symplectic integrators*, Phys. Lett. A, 150(5-7):262–268, 1990. 2.1